

Article

Higher-Order Spectral Analysis Combined with a Convolution Neural Network for Atrial Fibrillation Detection-Preliminary Study

Barbara Mika ^{*,†}  and Dariusz Komorowski [†] 

Faculty of Biomedical Engineering, Department of Medical Informatics and Artificial Intelligence, Silesian University of Technology, Roosevelt 40, 41-800 Zabrze, Poland; dariusz.komorowski@polsl.pl

* Correspondence: barbara.mika@polsl.pl

† These authors contributed equally to this work.

Abstract: The global burden of atrial fibrillation (AFIB) is constantly increasing, and its early detection is still a challenge for public health and motivates researchers to improve methods for automatic AFIB prediction and management. This work proposes higher-order spectra analysis, especially the bispectrum of electrocardiogram (ECG) signals combined with the convolution neural network (CNN) for AFIB detection. Like other biomedical signals, ECG is non-stationary, non-linear, and non-Gaussian in nature, so the spectra of higher-order cumulants, in this case, bispectra, preserve valuable features. The two-dimensional (2D) bispectrum images were applied as input for the two CNN architectures with the output AFIB vs. no-AFIB: the pre-trained modified GoogLeNet and the proposed CNN called AFIB-NET. The MIT-BIH Atrial Fibrillation Database (AFDB) was used to evaluate the performance of the proposed methodology. AFIB-NET detected atrial fibrillation with a sensitivity of 95.3%, a specificity of 93.7%, and an area under the receiver operating characteristic (ROC) of 98.3%, while for GoogLeNet results for sensitivity and specificity were equal to 96.7%, 82%, respectively, and the area under ROC was equal to 96.7%. According to preliminary studies, bispectrum images as input to 2D CNN can be successfully used for AFIB rhythm detection.

Keywords: atrial fibrillation; ECG; higher-order statistics; bispectrum; CNN; MIT-BIH atrial fibrillation database



Citation: Mika, B.; Komorowski, D. Higher-Order Spectral Analysis Combined with a Convolution Neural Network for Atrial Fibrillation Detection-Preliminary Study. *Sensors* **2024**, *24*, 4171. <https://doi.org/10.3390/s24134171>

Academic Editor: Loris Nanni

Received: 28 May 2024

Revised: 19 June 2024

Accepted: 25 June 2024

Published: 27 June 2024



Copyright: © 2024 by the authors. Licensee MDPI, Basel, Switzerland. This article is an open access article distributed under the terms and conditions of the Creative Commons Attribution (CC BY) license (<https://creativecommons.org/licenses/by/4.0/>).

1. Introduction

Atrial fibrillation (AFIB) is the most common persistent cardiac arrhythmia that poses a challenge in clinical practice and public health [1]. AFIB can lead to severe complications and typically reduce patients' quality of life and increase mortality as well as the cost to healthcare systems [2]. Scientific reports [3] show that the number of persons with atrial fibrillation in the United States in 2050 will exceed 10 million, while in the European Union, from 2010 to 2060, the number of adults 55 years and over with AFIB will more than double [1,4]. Estimates of current and future incidence and prevalence of atrial fibrillation are worrying and force the constant search for effective screening methods for AFIB detection.

Unlike other arrhythmias, the mechanisms of atrial fibrillation are more complex and have not yet been fully understood [5]. Modern theories link the underlying mechanism of atrial fibrillation with the reentry mechanism, which is not a disorder of impulse generation but its propagation; that is, the movement of an electrical impulse around an abnormal circuit repetitively. The depolarizing wave of the action potential leaves cells in the refractory state, unresponsive to further stimulation; hence, repeated stimulation of the same area requires a time-planned delay so that the next action potential can reenter the circuit and will not encounter cells unable to respond to the stimulation. In anatomic reentry, the boundaries of the circuit are physical cardiac structures [6]. Basic AFIB-maintaining mechanisms

can be pointing out local ectopic firing, single-circuit reentry, and multiple-circuit reentry [7]. According to the literature [2], AFIB is definite as “A supraventricular tachyarrhythmia with uncoordinated atrial electrical activation and consequently ineffective atrial contraction”.

Pathological features characteristic of AFIB diagnosis based on electrocardiogram documentation include [2,8]: “irregularly irregular R-R intervals (when atrioventricular conduction is not impaired), absence of distinct repeating P waves, and irregular atrial activations”. In compliance with [9], any arrhythmia recorded by a standard 12-lead ECG or a single-lead ECG tracing of at least 30 s of heart rhythm with AFIB characteristics, by convention, is diagnostic of clinical AFIB.

Although AFIB is not a fatal disease in itself if left untreated, it can result in serious health complications and, after some time, may cause stroke, heart failure, heart attack, and premature death [10]. Manual screening of AFIB on electrocardiogram is time-consuming and depends on the experience of the interpreting physician which can lead both to delay and differences in diagnosis and also mistakes and omissions [11]. Artificial intelligence (AI) with machine learning and deep learning techniques using electrocardiography (ECG) are powerful tools for detecting, classifying, and predicting AFIB seem to be a remedy for the above-mentioned human limitations.

Among the deep learning models developed for automatic AFIB detection and classification, we can find deep neural network (DNN) [12,13]; convolution neural network (CNN) [14,15]; recurrent neural network (RNN) [16,17]; long short-term memory network (LSTM) [18,19]; and hybrid (CNN + LSTM) network [20–23]. Their descriptions with advantages and disadvantages are widely presented and discussed in the work of Murat et al. [20], and Ebrahimi et al. [24]. The main advantage of CNN architectures pointed out in [20] is its strength in obtaining representative properties, so in our studies, CNN with bispectrum input was designed. CNNs can automatically learn representative features directly from the data itself, thus eliminating the need to extract distinctive features manually.

This paper focuses on AFIB detection based on convolution neural networks (CNNs) and higher-order statistics analysis (HOSA). Although many models have been developed using deep learning (DL) [25] to extract information from ECG signals, in this publication, we propose a new approach to detect atrial fibrillation based on higher-order cumulants. In our study, third-order spectra called bispectra are calculated for ECG signals from the MIT-BIH Atrial Fibrillation database and serve as an input to CNN. To our knowledge, such an approach has not yet been described and analyzed in the literature and may contribute to supporting the diagnosis of atrial fibrillation.

This work is organized as follows: in Section 2.1, the theoretical basis for higher-order spectral analysis is presented, and the concept of bispectrum is discussed. Section 2.2 is devoted to the MIT-BIH Atrial Fibrillation database, data preparation, feature extraction, and construction of convolution neural networks used for the AFIB classification and statistic measure. The following Sections 3–5 present the results, discussion, and conclusions.

2. Materials and Methods

2.1. Background on Higher-Order Spectral Analysis

Most biomedical signals present non-linear, non-stationary, and non-Gaussian characteristics [26]. These features cause the widely used primary tools of biomedical signal processing, such as correlation and spectral analysis, to quantify only some of the information available in the biomedical signals. Generally, higher-order spectra are Fourier transforms of higher-order statistics (HOS), moments, or cumulants. Moments are instead used for deterministic signals, while cumulants are for stochastic signals [27].

There are some reasons for using HOS to process biomedical signals to capture the desirable information [26]. Higher-order statistics of the Gaussian process are zero [28], so if the non-Gaussian signal is corrupted by the additive Gaussian noise, the transformation to the higher-order spectra (polyspectra) domain suppresses the Gaussian noise and, in consequence, return the signal with a higher signal-to-noise ratio (SNR) [27]. Because the polyspectra provide high noise immunity, they can be treated as a measure of no-

Gaussianity. The Fourier transform, the primary tool of power spectral analysis, transforms the signal from the time domain to the frequency domain. It quantifies the power distribution as a function of frequency but does not provide enough information about the phase relation between harmonic components. Hence, the degree of interaction, that is, phase coupling, usually originating from the non-linear source, cannot be assessed based on the power spectrum [29]. Due to polyspectra's ability to preserve amplitude and phase information, applying HOSA to process the biomedical signal is natural. Many scientists have applied HOSA with success to various biosignals, such as electroencephalogram (EEG) [30,31], electromyogram (EMG) [32], electrocardiogram (ECG) [33–35], heart rate variability (HRV) signals [36], image processing [37], and others.

This paper applied the HOSA technique to reveal hidden information from ECG signals. In particular, the third-order spectrum called the bispectrum was used to capture the impact of atrial fibrillation on ECG and served as an input to CNN.

2.1.1. Moments and Cumulants

Let $X \in \mathcal{R}^N$ represent the random variable. If the probability density function $f(t)$ of the variable X is Gaussian, the random variable X is fully characterized by the mean (first-order statistic) and the covariance (second-order statistic). For the continuous random variable X with the probability density function $f(t)$ the characteristic function $\phi(t)$ is defined as (1)

$$\phi(t) = E(e^{jXt}) \iff \phi(t) = \int_{-\infty}^{\infty} f(t) \cdot e^{jxt} dt, \quad (1)$$

where $E(\cdot)$ denotes the expectation value, $f(t)$ the probability density function of the random variable X . The function $\phi(t)$ is called the characteristic function or the moment-generating function. The characteristic function $\phi(t)$ can be expressed as a Maclaurin series expansion (2)

$$\phi(t) = 1 + \sum_{k=1}^{\infty} \frac{m_k}{k!} (jt)^k, \quad (2)$$

with the coefficients $m_k = \frac{1}{j^k} \phi^{(k)}(0) = E(X^k)$ of k -order (for $k \in \{1, 2, 3, \dots\}$) moments of random variable X where (k) denotes the k -order derivative of the function $\phi(t)$. Higher-order moments are usually used to define the distribution more precisely [38].

Because the higher-order moments of Gaussian distribution are constant but not zero, the natural logarithm of characteristic function is used. The coefficients of expansion of the function $g(t) = \ln(\phi(t))$, where $\phi(t)$ is a characteristic function (i.e., moment-generating function), in the Maclaurin series (3) are known as cumulants (c_k).

$$g(t) = \sum_{k=1}^{\infty} \frac{c_k}{k!} (jt)^k, \quad (3)$$

where $c_k = \frac{1}{j^k} g^{(k)}(0)$ is a k -order cumulant, and (k) denotes the k -order derivative of the function $g(t)$. The function $g(t)$ is called a cumulant-generating function. Based on successive derivation of function $g(t)$, the first three cumulants are equal to

$$c_1 = EX \quad \wedge \quad c_2 = E(X - EX)^2 \quad \wedge \quad c_3 = E(X - EX)^3,$$

that is,

$$c_1 = m_1 \quad \wedge \quad c_2 = m_2 - (m_1)^2 \quad \wedge \quad c_3 = m_3 - 3m_2m_1 + 2(m_1)^3,$$

so the first cumulant is expected value (mean) of random variable X and the second and third cumulants are central moments of the second (variance) and third order, respectively. Cumulants on a higher order than two are zero for the Gaussian distribution [28].

Let $X = [X_1, X_2, X_3, \dots, X_p]^T$ be p -dimensional random variable $X \in \mathcal{R}^{px1}$. The characteristic function of X is then definite as (4)

$$\Phi(\mathbf{t}) = E(e^{j(X,\mathbf{t})}) \iff \Phi(\mathbf{t}) = E\left(\prod_{k=1}^p e^{jX_k t_k}\right), \tag{4}$$

where $\mathbf{t} = [t_1, t_2, \dots, t_p]^T$, (\mathbf{t}, X) is a scalar product of vectors X , and \mathbf{t} . It is said that the vector X admits moments of order n if $E(|X|^n) < \infty$, where $|X| = \sqrt{\sum_{i=1}^p x_i^2}$ denotes the norm in the \mathcal{R}^p space. In such a case, the Φ function is n -time differentiable and the k -order ($k \leq n$) moments ($M^{(k)}$) exist and they are definite as (5) [39]

$$\begin{aligned} \forall_{(i_1, \dots, i_k) \in \mathcal{A}} M^{(k)}(X_{i_1}, \dots, X_{i_k}) &= E(X_{i_1} \cdot X_{i_2} \cdot \dots \cdot X_{i_k}) \\ &\iff \\ \forall_{(i_1, \dots, i_k) \in \mathcal{A}} M^{(k)}(X_{i_1}, \dots, X_{i_k}) &= \frac{1}{j^k} \frac{\partial^k \Phi}{\partial t_{i_1} \dots \partial t_{i_k}}(0), \end{aligned} \tag{5}$$

where the set \mathcal{A} contains all the k -element sequences created from the elements of the set $\{1, 2, \dots, p\}$. In addition, the function Φ is continuous and $\Phi(0) = 1$ with non-zero values in the neighborhood of $0 \in \mathcal{R}^p$ so the function-generating cumulants can be written as (6)

$$\Psi(\mathbf{t}) = \ln(E(e^{j(X,\mathbf{t})})). \tag{6}$$

Because of $E(|X|^n) < \infty$, function Ψ is n -time differentiable and the joint cumulants of k -order ($k \leq n$) ($C^{(k)}$) are definite by (7)

$$\forall_{(i_1, \dots, i_k) \in \mathcal{A}} C^{(k)}(X_{i_1}, \dots, X_{i_k}) = \frac{1}{j^k} \frac{\partial^k \Psi}{\partial t_{i_1} \dots \partial t_{i_k}}(0). \tag{7}$$

For multiple dimensional random variables $X \in \mathcal{R}^p$, ($X = [X_1, X_2, X_3, \dots, X_p]^T$) the relationship between its cumulants and moments of k -order ($k \leq p$) could be established by the Leonov and Shiryaev formula [39] (8)

$$\begin{aligned} C^{(k)}(X_{i_1}, \dots, X_{i_k}) &= \\ &= \sum_{\pi \in Pr(\{1, \dots, k\})} (-1)^{|\pi|-1} (|\pi|-1)! \prod_{\mathcal{B} \in \pi} E\left(\prod_{i \in \mathcal{B}} X_i\right), \end{aligned} \tag{8}$$

where set $Pr(\{1, \dots, k\})$ includes all the blocks of k -order partitions, π runs through all blocks of set $Pr(\{1, \dots, k\})$, $|\pi|$ denotes the order (number of parts) for partition in the set π , and $\mathcal{B} \in \pi$ the partition from the set π .

Below, we present an example of $Pr(\{1, 2\})$ for $k = 2$ (9) and $Pr(\{1, 2, 3\})$ for $k = 3$ (10), where ($|\pi_i| = i$ for $i \in \{1, 2, 3\}$).

$$Pr(\{1, 2\}) = \left\{ \underbrace{\{1, 2\}}_{\mathcal{B}_1}; \underbrace{\left\{ \underbrace{\{1\}}_{\mathcal{B}_1}, \underbrace{\{2\}}_{\mathcal{B}_2} \right\}}_{\mathcal{B}_1, \mathcal{B}_2} \right\} \tag{9}$$

$$\begin{aligned} Pr(\{1, 2, 3\}) &= \left\{ \underbrace{\{1, 2, 3\}}_{\mathcal{B}_1}; \right. \\ &\left. \underbrace{\left\{ \underbrace{\{1\}}_{\mathcal{B}_1}, \underbrace{\{2, 3\}}_{\mathcal{B}_2} \right\}}_{\mathcal{B}_1, \mathcal{B}_2}; \underbrace{\left\{ \underbrace{\{2\}}_{\mathcal{B}_2}, \underbrace{\{1, 3\}}_{\mathcal{B}_3} \right\}}_{\mathcal{B}_2, \mathcal{B}_3}; \underbrace{\left\{ \underbrace{\{3\}}_{\mathcal{B}_3}, \underbrace{\{1, 2\}}_{\mathcal{B}_1} \right\}}_{\mathcal{B}_3, \mathcal{B}_1}; \right. \\ &\left. \underbrace{\left\{ \underbrace{\{1\}}_{\mathcal{B}_1}, \underbrace{\{2\}}_{\mathcal{B}_2}, \underbrace{\{3\}}_{\mathcal{B}_3} \right\}}_{\mathcal{B}_1, \mathcal{B}_2, \mathcal{B}_3} \right\}. \end{aligned} \tag{10}$$

Based on (8)–(10) for $X = [X_1, X_2]$, the second-order cumulant can be expressed by (11)

$$C(X_1, X_2) = E(X_1 X_2) - E(X_1)E(X_2), \quad (11)$$

while the third-order cumulant is given by (12)

$$C(X_1, X_2, X_3) = E(X_1 X_2 X_3) - E(X_1)E(X_2 X_3) - E(X_2)E(X_1 X_3) - E(X_3)E(X_1 X_2) + 2E(X_1)E(X_2)E(X_3). \quad (12)$$

If we assume that $EX_i = 0$ for $i \in \{1, 2, 3\}$, then the Formulas (11) and (12) simplify to

$$C(X_1, X_2) = E(X_1 X_2) \text{ and } C(X_1, X_2, X_3) = E(X_1 X_2 X_3). \quad (13)$$

For time-dependent, real-valued stationary p -dimensional random process $\mathcal{X} = [X(t), X(t + \tau_1), X(t + \tau_2), \dots, X(t + \tau_{p-1})]$, with the time shift $\tau_1, \tau_2, \dots, \tau_{p-1}$, respectively. The i -th shift for ($i \in \{1, 2, \dots, p-1\}$) is equal to $i \cdot T_s$ where T_s denotes the sampling period. Hence, the p -order cumulant ($C_{p,\mathcal{X}}$) is defined as the p -order joint cumulant of $X(t), X(t + \tau_1), X(t + \tau_2), \dots, X(t + \tau_{p-1})$, given by (14) [40]

$$C_{p,\mathcal{X}} = C(X(t), X(t + \tau_1), X(t + \tau_2), \dots, X(t + \tau_{p-1})). \quad (14)$$

The second- and third-order cumulants of zero-mean random variable \mathcal{X} can be expressed as follows:

$$C_{2,\mathcal{X}}(\tau) = E(X(t)X(t + \tau)) \quad (15)$$

$$C_{3,\mathcal{X}}(\tau_1, \tau_2) = E(X(t)X(t + \tau_1)X(t + \tau_2)).$$

If the process \mathcal{X} is Gaussian, all the cumulants are zero [28], so the cumulants are also a measure of the deviation from the Gaussian distribution.

2.1.2. Bispectrum

Higher-order spectra are defined with the aid of higher-order moments or cumulants. They are Fourier transforms of higher-order statistics. Applying the Fourier transform for the first three cumulants, we obtain the power spectrum, bispectrum, and trispectrum, respectively [27].

Assuming that the cumulant sequences are absolutely summable (16)

$$\sum_{\tau_1=-\infty}^{+\infty} \cdots \sum_{\tau_{p-1}=-\infty}^{+\infty} |C_{p,\mathcal{X}}(\tau_1, \tau_2, \dots, \tau_{p-1})| < +\infty \quad (16)$$

the p th-order polyspectrum ($S_{p,\mathcal{X}}$) is definite as $(p-1)$ -order-dimensional discrete-time Fourier transform (\mathcal{DTFT}) of the p th-order cumulant as follows (17):

$$\begin{aligned} S_{p,\mathcal{X}}(f_1, f_2, \dots, f_{p-1}) &= \mathcal{DTFT}(C_{p,\mathcal{X}}(\tau_1, \tau_2, \dots, \tau_{p-1})) = \\ &= \sum_{\tau_1=-\infty}^{+\infty} \cdots \sum_{\tau_{p-1}=-\infty}^{+\infty} C_{p,\mathcal{X}}(\tau_1, \tau_2, \dots, \tau_{p-1}) \cdot e^{-j \sum_{i=1}^{p-1} 2\pi f_i \tau_i}. \end{aligned} \quad (17)$$

For $p = 3$, we obtain the bispectrum ($S_{3,\mathcal{X}}(f_1, f_2) = B(f_1, f_2)$) as the double \mathcal{DTFT} of the third-order cumulant $C_{3,\mathcal{X}}$ (18)

$$B(f_1, f_2) = \sum_{\tau_1=-\infty}^{+\infty} \sum_{\tau_2=-\infty}^{+\infty} C_{3,\mathcal{X}}(\tau_1, \tau_2) \cdot e^{-j \sum_{i=1}^2 2\pi f_i \tau_i}. \quad (18)$$

A bispectrum is a function of two frequencies f_1, f_2 , and their couple (f_1, f_2) is called a bi-frequency. Because of the symmetry relationships in the cumulants graph, only those bi-frequencies inside the triangular region (19) are considered non-redundant.

$$f_2 \geq 0 \wedge f_1 \leq f_2 \wedge (f_1 + f_2) \leq \frac{1}{2}F_s \quad (19)$$

where F_s is the sampling frequency.

2.2. AFIB Detection Stage

The proposed method for detecting AFIB rhythms in the ECG signal consists of the following steps: data preparation, feature extraction, and AFIB classification. Feature extraction is based on HOSA, and two architectures of neural networks are proposed for classification: a serial CNN network (further referred to as AFIB-NET) and a pre-trained GoogLeNet network (GNN) [41] with some modifications. The details of each stage are provided in the following subsections. To evaluate the performance of the proposed method, the MIT-BIH Atrial Fibrillation Database (AFDB) (<https://physionet.org/content/afdb/1.0.0/> (accessed on 24 June 2024)) was used [42].

2.2.1. MIT-BIH Database

The AFDB database includes 25 long-term ECG recordings of human subjects with atrial fibrillation. Of these, 23 (two of the ECG signals are not provided) records were used in our studies. Each record (of 23) contained two ECG signals sampled at 250 samples per second with 12-bit resolution over a range of ± 10 millivolts. Each recording is about 10 h long and has a bandwidth of approximately 0.1 to 40 Hz. AFDB provides the rhythm annotations files, which include 605 annotated episodes, with rhythm annotations of types AFIB (atrial fibrillation), AFL (atrial flutter), J (Nodal (junctional) rhythm), and N used for all other rhythms. AFDB contains a total of 1,686,797.776 (468 h) s of ECG signals (843,398.888 s (234 h) for one ECG lead). The details about time duration for the four available rhythms are included in Table 1.

Table 1. Time duration of the AFIB, AFL, Nodal, N (other) rhythms for analyzed ECG signals from MIT-BIH Atrial Fibrillation database.

Episode	Nº	Min [s]	Max [s]	Mean [s]	Total [s]
AFIB	291	1.684	36,822.864	1155.436	336,231.984
AFL	14	3.532	3390.912	419.794	5877.116
Nodal	12	1.524	86.016	27.582	330.980
N (other)	288	4.252	30,981.372	1739.440	500,958.808

2.2.2. Data Preparation

In the first stage of data preparation, ECG fragments annotated as AFIB and N (used to indicate all other rhythms) were extracted from each signal of the AFIB MIT-BIH database. Each AFIB and N of the ECG fragment was divided into 5 s segments because it is a long enough time to detect the change in heart rhythm. ECG fragments with AFIB and N rhythms that were less than 5 s long were omitted. As a result of such division, we obtained 134,212 5 s ECG fragments with the AFIB rhythm and, simultaneously, 200,092 5 s fragments with N (all other) rhythms. Fragments of ECG signals with less than 5 s, 582 for AFIB and 574 for N rhythms, were omitted. The bispectrum was then calculated for each 5 s segment of the ECG signals. Bispectra were calculated using the Higher-Order Spectral Analysis (HOSA) MATLAB Toolbox [43]. The HOSA Matlab toolbox proposes two non-parametric methods to estimate the higher-order spectrum (in our case, bispectrum): direct (based on fast Fourier transform (FFT)) and indirect. We checked both methods. The FFT length for computing the bispectrum was set to 512. We chose the direct method for bispectrum

estimation based on the preliminary results. The details of algorithms and implementation of direct and indirect methods for bispectrum estimation can be found in the literature [43].

2.2.3. Feature Extraction

In line with a review of the literature in which the frequency range of atrial activities was examined, it is concluded that it is not precisely defined but belongs to the range of approximately 3 to 12 Hz [44–50]; therefore, for further analysis, we used fragments of bispectra from 0.5 to 12 Hz. The examples of ECG signal and their spectra and bispectra for both AFIB and N rhythms are depicted in Figures 1 and 2, respectively. The absolute value and phase of the bispectrum are presented as a contour obtained for the level equal to 20.

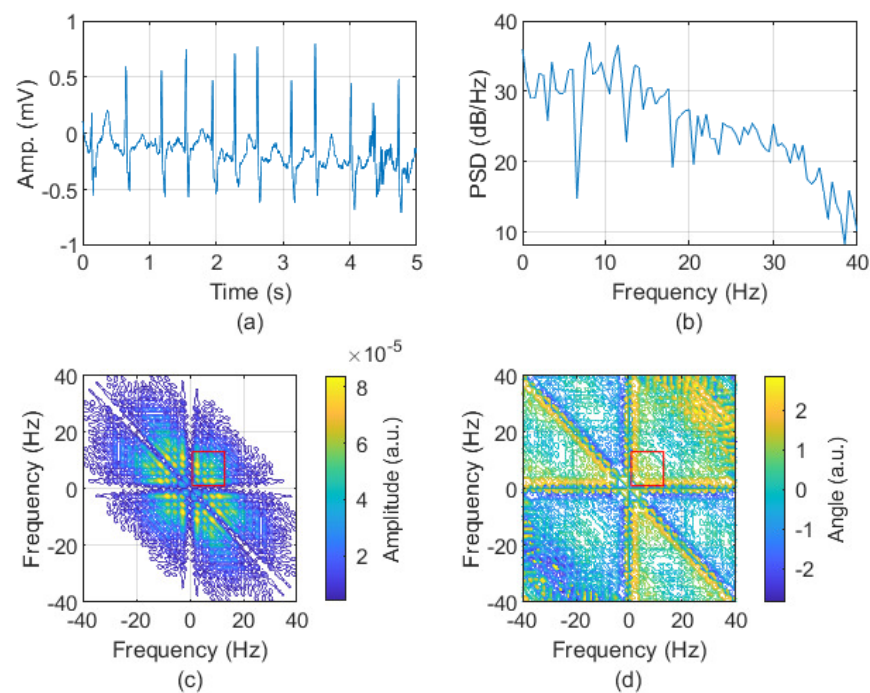


Figure 1. The 5 s length fragment of ECG with AFIB rhythms (signal: 04048 AFDB, channel 1, the first 5 s of the signal containing AFIB rhythm) (a). The spectrum (calculated by Welch method [51,52]) (b). The absolute value (c) and phase (d) of bispectrum. The red rectangle indicates the frequencies in the range 0.5 to 12 Hz.

Both the absolute value and the phase of bispectra in the 0.5 to 12 Hz range were normalized into the range between 0 and 1, corresponding to a conversion into a gray image. The min–max normalization method was applied in the area corresponding to the analyzed frequency range. The two-dimensional images representing the absolute value of bispectra size 24×24 were used as the input for AFIB-NET. The sample images corresponded to bispectra in the absolute frequency range of 0 to 40 Hz are shown in the Figures 3 and 4. The fragments marked by the red rectangle (after normalization in the zone of interest) were used to train the AFIB-NET network. Figure 5 shows the histograms of pixel value for the normalized data (gray image) corresponding to the amplitude of the bispectrum of the ECG signals with AFIB and N rhythms (for ECG in Figures 1a and 2a).

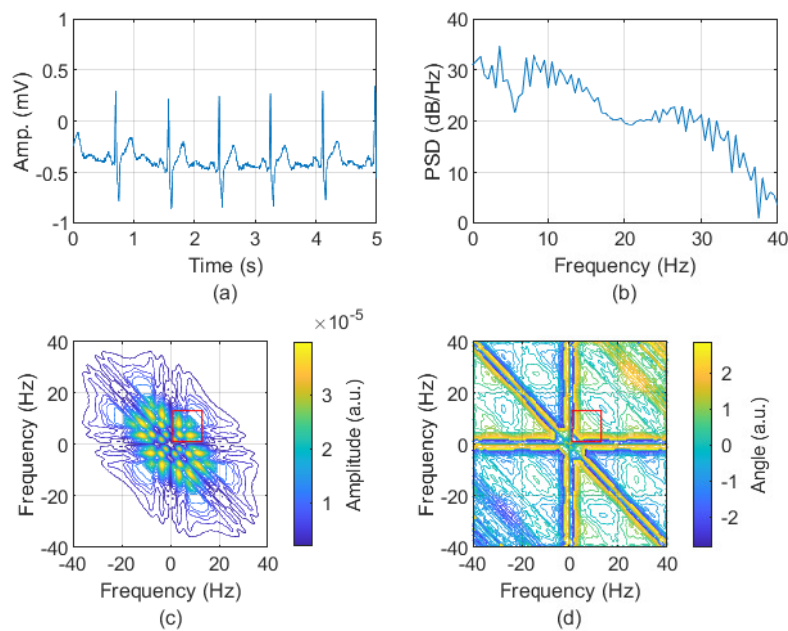


Figure 2. The 5 s length fragment of ECG with N rhythms (signal: 04048 AFDB, channel 1, the first 5 s of the signal containing N rhythm) (a). The spectrum (calculated by Welch method [51,52]) (b). The absolute value (c) and phase (d) of bispectrum. The red rectangle indicates the frequencies in the range 0.5 to 12 Hz.

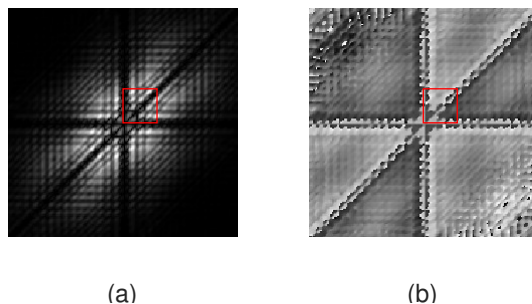


Figure 3. The gray images (absolute value (a) and phase (b)) obtained after converting the bispectrum of the fragment of ECG with the AFIB rhythm. The red rectangle (a) marks the area used as the input of the AFIB-NET. The size of images corresponds to the absolute frequency range of 0 to 40 Hz (signal: 04048 AFDB, channel 1, the first 5 s of the signal containing AFIB rhythm).

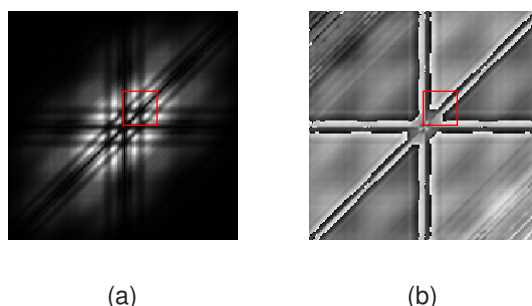


Figure 4. The gray images (absolute value (a) and phase (b)) obtained after converting the bispectrum of the fragment of ECG with N rhythm. The red rectangle (a) marks the area used as the input of the AFIB-NET. The size of images corresponds to the absolute frequency range of 0 to 40 Hz (signal: 04048 AFDB, channel 1, the first 5 s of the signal containing N rhythm).

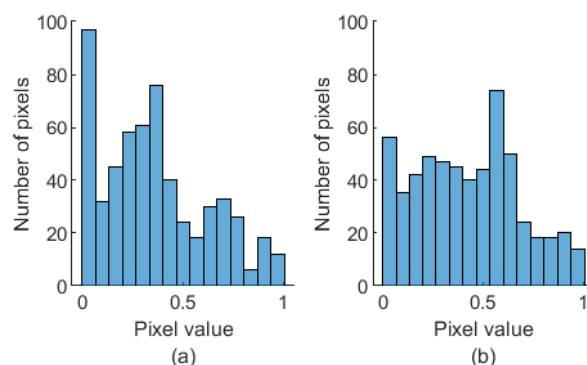


Figure 5. The histograms of the images correspond to the absolute value of the bispectrum of the ECG signal with the AFIB rhythm (a) (signal: 04048 AFDB, channel 1, the first 5 s of the signal containing AFIB rhythm) and the N rhythm (b) (signal: 04048 AFDB, channel 1, the first 5 s of the signal containing N rhythm), respectively.

Since the GNN uses the three color channels (RGB) image with a size of $224 \times 224 \times 3$, the input image preparation was made as follows: we used the fragments of bispectra from 0.5 to 14 Hz (the range of the frequencies was extended to 14 Hz because of GNN input layer size), which corresponds to the image of size $28 \times 28 \times 1$; this image was replicated 64 times (8×8), and copied to each of the RGB layers.

2.2.4. Classification

Two different architectures of deep neural networks were used for the classification. The first approach used the series AFIB-NET, whose detailed structure is presented in Table 2, and the second used modified GNN. The modification considered a change in the number of classes and the adaptation of the network output layer for the classification task being performed. The proposed method was evaluated using the bispectrum images corresponding to the ECG signals with AFIB and N rhythms obtained by the methods mentioned above. We considered about 2000 to 18,000 images (half and half AFIB and N class) randomly chosen from all datasets (134,212 images corresponded to AFIB and 200,092 to N (other) rhythms)). The 70% of the obtained bispectra (images) were used to train the AFIB-NET, the 10% was used to validate the network, and the remaining 20% was used to test the networks.

The AFIB-NET was trained for 40 epochs with a mini-batch size (MBS) equal to 32. The initial learning rate (ILR) was calculated using the following formula: $ILR = 0.1 \cdot miniBatchSize / 128$, resulting in an ILR value equal to 0.25. The GNN was trained for 60 epochs with the initial learning rate equal to 0.0001. The code was written in MATLAB 2022a and ran in the workstation equipment with processor Intel(R) Core(TM) i9-10980XE 3.00 GHz, 128 GB RAM, and graphics card NVIDIA Quadro RTX 5000 with 16 GB memory.

Table 2. The AFIB-NET neural network architecture. The activation dimension (Activations) is given in the following format: $S \times S \times C \times B$, where labels mean: S-spatial, C-channel, and B-batch observation.

Layer	Type	Filter Size	Number of Filters	Stride	Activations	Number of Learnables
1	Image Input	-	-	-	$24 \times 24 \times 1 \times 1$	0
2	Convolution	3×3	8	[1 1]	$24 \times 24 \times 8 \times 1$	80
3	Batch Normalization	-	-	-	$24 \times 24 \times 8 \times 1$	16
4	ReLU	-	-	-	$24 \times 24 \times 8 \times 1$	0
5	Max Pooling	-	-	[1 1]	$23 \times 23 \times 8 \times 1$	0
6	Convolution	3×3	16	[1 1]	$23 \times 23 \times 16 \times 1$	1168
7	Batch Normalization	-	-	-	$23 \times 23 \times 16 \times 1$	32

Table 2. Cont.

Layer	Type	Filter Size	Number of Filters	Stride	Activations	Number of Learnables
8	ReLu	-	-	-	$23 \times 23 \times 16 \times 1$	0
9	Ma × Pooling	-	-	[1 1]	$22 \times 22 \times 16 \times 1$	0
10	Convolution	3×3	32	[1 1]	$22 \times 22 \times 32 \times 1$	4640
11	Batch Normalization	-	-	-	$22 \times 22 \times 32 \times 1$	64
12	ReLu	-	-	-	$22 \times 22 \times 32 \times 1$	0
13	Max Pooling	-	-	[1 1]	$11 \times 11 \times 32 \times 1$	0
14	Convolution	3×3	64	[2 2]	$11 \times 11 \times 64 \times 1$	18,496
15	Batch Normalization	-	-	-	$11 \times 11 \times 64 \times 1$	128
16	ReLu	-	-	-	$11 \times 11 \times 64 \times 1$	0
17	Max Pooling	-	-	[1 1]	$5 \times 5 \times 64 \times 1$	0
18	Convolution	3×3	128	[2 2]	$5 \times 5 \times 128 \times 1$	73,856
19	Batch Normalization	-	-	-	$5 \times 5 \times 128 \times 1$	256
20	ReLu	-	-	-	$5 \times 5 \times 128 \times 1$	0
21	Fully Connected	-	-	-	$1 \times 1 \times 2 \times 1$	6402
22	Softmax	-	-	-	$1 \times 1 \times 2 \times 1$	0
23	Classification Output	-	-	-	$1 \times 1 \times 2 \times 1$	0

2.3. Statistical Measures Applied for the Classifiers Assessment

Several statistical measures were applied for the proposed AFIB-NET and modified GoogLeNet network to evaluate the power of the proposed method dedicated to AFIB detection.

Sensitivity (also known as recall, or true positive rate (TPR)):

$$TPR = \frac{TP}{TP + FN}. \quad (20)$$

Specificity (true negative rate (TNR)) understood as:

$$TNR = \frac{TN}{TN + FP}. \quad (21)$$

The precision of positive predictive value:

$$PPV = \frac{TP}{TP + FP}. \quad (22)$$

The precision of negative predictive value:

$$NPV = \frac{TN}{TN + FN}. \quad (23)$$

Prevalence:

$$PV = \frac{TP + FN}{TP + TN + FN + FP}. \quad (24)$$

Accuracy

$$ACC = \frac{TP + TN}{TP + FN + FP + TN} = sensitivity \cdot PV + specificity \cdot (1 - PV). \quad (25)$$

The likelihood ratio of positive values:

$$LR+ = \frac{sensitivity}{1 - specificity} \quad (26)$$

and the likelihood ratio of negative values:

$$LR- = \frac{1 - sensitivity}{specificity} \tag{27}$$

Area (AUC) under receiver operating characteristic (ROC), and F1-score

$$F1 = \frac{2 \cdot precision \cdot sensitivity}{precision + sensitivity} \tag{28}$$

for rhythm classes AFIB ($F1_{AFIB}$, for precision = PPV) and N ($F1_N$, for precision = NPV). TP—true positive, FN—false negative, FP—false positive, TN—true positive parameters referred to the confusion matrix obtained for the process of classification.

3. Results

The statistical measures definite in Section 2.3 were calculated for AFIB-NET and GNN and are summarized in Table 3. The confusion matrices for the proposed AFIB-NET and the modified GNN in the AFIB classification are presented in Figures 6 and 7, respectively. Next to the confusion matrix, we can see vertically (in the blue boxes) the sensitivity and specificity values expressed in percentage. The precision of positive (PPV) and negative (NPV) predictive values are presented in the horizontal blue boxes under the confusion matrix. The values of these parameters are also summarized in Table 3.

Table 3. Classifier evaluation parameters: sensitivity, specificity, positive predictive value (PPV), negative predictive value (NPV), prevalence (PV), accuracy (ACC), the likelihood ratio of positive value (LR+), the likelihood ratio of negative value (LR-), the area under ROC curve (AUC), and F-score for AFIB and N class for both the AFIB-NET and GNN.

Measure	AFIB-NET	GooLeNet (GNN)
Sensitivity (TPR)	0.953	0.967
Specificity (TNR)	0.937	0.824
PPV	0.938	0.846
NPV	0.952	0.961
PV	0.500	0.500
ACC	0.945	0.896
LR+	15.127	5.494
LR-	0.050	0.040
AUC	0.983	0.967
$F1_{AFIB}$	0.945	0.902
$F1_N$	0.952	0.964

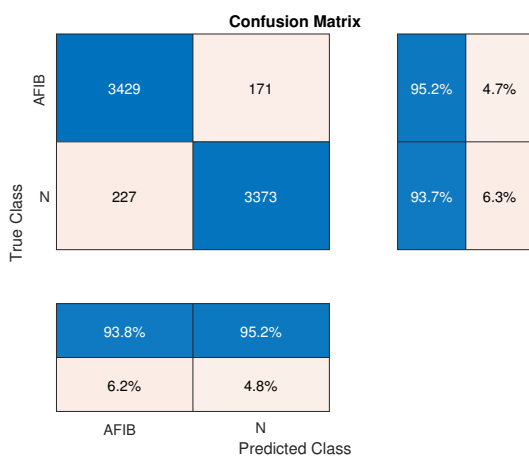


Figure 6. Confusion matrix for the proposed AFIB-NET in AFIB classification. The vertical blue boxes next to the confusion matrix present the sensitivity (TPR) and specificity (TNR) values, while the horizontal blue boxes below the confusion matrix state the precision of the positive (PPV) and negative (NPV) predictive values, respectively.

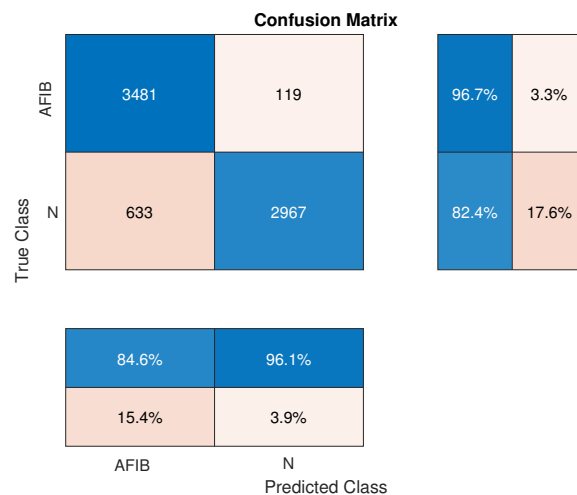


Figure 7. Confusion matrix for modified GNN in AFIB classification. The vertical blue boxes next to the confusion matrix present the sensitivity (TPR) and specificity (TNR) values, while the horizontal blue boxes below the confusion matrix state the precision of the positive (PPV) and negative (NPV) predictive values, respectively.

In addition, Figure 8 presents ROC curve plots with the mark of the net model operating point and the calculated area under the ROC curve for the AFIB class for both AFIB-NET and GoogLeNet.

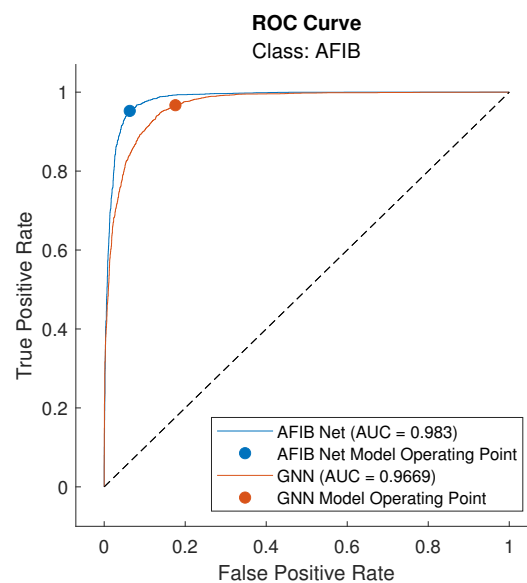


Figure 8. Receiver operating characteristic (ROC) curves of AFIB class for AFIB-NET and GNN, with marked net model operating points and areas under ROC (AUC) value. *True Positive Rate* means sensitivity, while *False Positive Rate* states 1-specificity.

4. Discussion

4.1. Main Findings of the Study

A good classification model is one that minimizes the number of errors (FP and FN in the confusion matrix). However, the cost of these errors is not always the same, that is, not in all applications. From the medical point of view, it is safer to treat a healthy person as sick (FP) and perform further diagnostic tests to exclude the disease than to treat a sick person as healthy (FN) and not undertake any treatment. Therefore, when analyzing both confusion matrices for AFIB detection, the $FP > FN$ situation is acceptable, which, in turn, views lower precision in favor of higher sensitivity. Such a situation occurs for both

analyzed networks (Table 3). However, for GNN, the difference is much higher in the benefit of sensitivity, especially for the precision of positive predictive value (PPV).

If we assume that both precision and sensitivity are essential, we can use the F1 metric, which is the harmonic mean of sensitivity and precision and provides information about the balance between sensitivity and precision maintained by the model. A higher F1 score suggests a better balance between sensitivity and precision, indicating a more effective model. After analyzing the results obtained in this context, we found that the AFIB-NET model is more effective than GNN. $F1_{AFIB}$ and $F1_N$ for AFIB-NET differ by only 0.007, so the model presents a good high balance. At the same time, GNN is a better-balanced model in terms of sensitivity and precision for class N ($F1_N = 0.964$) than for class AFIB ($F1_{AFIB} = 0.902$), which means that GNN more often classified the person with N rhythm as a person with AFIB, and such feature from a medical point of view can be acceptable.

Based on the sensitivity and specificity measures, we can determine the likelihood ratio of positive and negative predicting values, that is, AFIB or N rhythms detection, respectively. Assuming, in accordance with the literature [53,54], that the results obtained from the model have a real diagnostic value for LR+, about 10 and more, and LR-, about 0.1 and less, the results (LR+ = 15.127 and LR- = 0.050) obtained for AFIB-NET would indicate a greater diagnostic value in relation to GNN. In this case, the results obtained for GNN would classify this model only as applicable.

Sensitivity and specificity are the measures that are the basis for the construction of ROC curves. A good decision rule is one that maximizes both of these measures. We can use ROC curves to find the optimal cut-off model operating point for a given model, that is, the point at which both of these measures reach their maximum value simultaneously. ROC curves illustrate the relationship between the sensitivity and specificity of a given model and allow for a comprehensive assessment of the decision rule of the constructed model [55]. In Figure 8 we can compare the ROC curves for AFIB-NET and GNN. The model operating point for AFIB-NET is closer to point (0,1), which means the maximum values for sensitivity and specificity.

A widely used approach is to calculate the area under the ROC curve (AUC) and treat it not only as a measure of the goodness and rightness of a given model but also as a tool for assessing and comparing classification models. The AUC parameter takes a value in the range [0, 1]. The higher the AUC value, the better the model. For the models considered in this work, the AUC parameter was also determined (Table 3), and its value is equal to 0.983 for AFIB-NET and 0.967 for GNN, so it could be concluded that both models are correct, but the AFIB-NET is slightly better.

The results confirm the potential of the bispectral analysis of ECG signals and the convolution neural networks applied to AFIB detection. One of the problems in automatic ECG analysis is the significant difference in ECG signal morphology between patients or groups of patients and even within the same person [26,56]. For this reason, higher-order spectra, as the spectral representation of higher-order cumulants or moments of the given signal, in our case, bispectrum seems to be a good choice. Bispectrum extracts the non-Gaussian, non-linearity characteristics from ECG signals and reduces the variation in morphology changes. In addition, the bispectrum preserves the phase relationships between harmonic components.

Based on frequency ranges reported to the AFIB rhythm [44–50], we present the preliminary results of AFIB detection for the bispectrum frequency band 0.5–12 Hz, which are promising, but still, in the future, we would like to check if or how the frequency band influences the analysis's effectiveness. In the future, we are planning to repeat the proposed methodology for the bispectrum with a higher resolution. In this study, we also tested not only the amplitude bispectrum as the input to the CNN but also the phase bispectrum images and the combined amplitude and phase bispectrum images. However, the obtained results were not satisfactory, and this approach demands further investigation. The conducted learning and testing processes of CNNs were time-consuming and lasted from some to several dozen hours for one set of parameters and one network architecture.

4.2. Comparison to Other Algorithms

In line with the summaries and results, which can be found in [57–59] and other literature (Table 4), we present a comparison of the classification by the proposed technique with the chosen machine learning, deep learning-based methods, and other algorithms developed for detecting the AFIB rhythm using the MIT-BIH Atrial Fibrillation database. Nevertheless, it should be noted that such a comparison is quite difficult to interpret. A very substantive comparison of AFIB detection results and an interesting discussion on the difficulties and interpretation of comparing the quality of atrial fibrillation detection results for different algorithms are presented in the 2023 Yang et al. [59].

The effectiveness of the proposed procedure for AFIB detection based on the bispectrum images corresponds to those presented in Table 4, in terms of the most often presented measures: sensitivity and specificity. However, the other measures presented in Table 3, discussed earlier are in favor of the bispectrum, which, used as the input to the CNN, has a large potential for automated detection of atrial fibrillation.

Table 4. Comparison of sensitivity and specificity of chosen deep learning-based methods and other algorithms for AFIB rhythm detection for ECG signals using the MIT-BIH Atrial Fibrillation database.

Method Proposed by	Sensitivity (%)	Specificity (%)
RADHAKRISHNAN et al. (2021) [58]	99.17	98.90
Marsanova et al. (2020) [60]	96.32	98.61
Wang et al. (2020) [61]	98.70	98.90
Mousavi et al. (2019) [57]	99.53	99.26
Xia et al. (2018) (STFT) [14]	98.34	98.24
Xia et al. (2018) (SWT) [14]	98.79	97.87
Kumar et al. (2018) [62]	95.80	97.60
Tripathy et al. (2017) [63]	97.77	98.67
Asgari et al. (2015) [64]	97.00	97.10
Lee et al. (2013) (RMSSD) [65]	90.49	94.17
Lee et al. (2013) (ShE) [65]	74.15	96.81
Lee et al. (2013) (SamE) [65]	97.26	99.61
Huang et al. (2011) [66]	96.10	98.10
Tateno et al. (2001) [67]	94.40	97.20
AFIB (Proposed work)	95.30	96.70
GNN (Proposed work)	93.70	82.00

4.3. Strength and Limitations

This research's novelty is using bispectrum images as input to CNN to automate AFIB detection. In favor of bispectrum compared to other techniques is bispectrum's ability to capture the non-Gaussian, non-linear nature of ECG signals. Moreover, bispectrum can identify the phase coupling, usually originating from the non-linear source, and reduce the variation in morphology changes in ECG. The presented preliminary studies confirm that bispectrum images are a good choice for input to the CNN classifier for AFIB detection, but further investigations are required.

The main limitation of this study is that only one ECG database, including two-lead ECG, was used to test the performance of the proposed method. In this work, we tested the ECG signals of the MIT-BIH Atrial Fibrillation database. It is a very good database that is widely used and allows for the comparison of results, but there is a possibility that the signals are somehow correlated. Although the classification was performed with the good practice of using the training, validation, and testing set as the next stage of our studies, we also intend to test the proposed methodology on new data from other ECG databases.

5. Conclusions

To the best of our knowledge, this is the first study that combines the methodology of higher-order spectrum (bispectrum) and convolution neural network for the automated detection of AFIB in ECG signals. During the classic assessment of the occurrence of AFIB, these three main features “irregularly irregular R-R intervals (when atrioventricular conduction is not impaired), absence of distinct repeating P waves, and irregular atrial activations”

are taken into account. As the bispectrum suppresses the observed features caused by the morphological changes in ECG, it gives the opportunity to catch the variability contributed by the AFIB. The proposed model uses a bispectrum of ECG signal as an input for the proposed convolution neural network AFIB-NET and detects atrial fibrillation with a sensitivity of 0.953, specificity of 0.937, and AUC equal to 0.983. The obtained results for AFIB-NET confirm the effectiveness of the use of bispectra in combination with CNN for detecting AFiB. As the future direction of our studies, we plan to test other bands of frequency and resolution for bispectra images and to test the proposed method for additional ECG databases. We also intend to extend the AFIB-NET classifier for more ECG rhythms.

Author Contributions: Conceptualization, B.M. and D.K.; methodology, B.M. and D.K.; software, D.K.; validation, B.M. and D.K.; formal analysis, B.M. and D.K.; investigation, B.M. and D.K.; writing—original draft preparation, B.M. and D.K.; writing—review and editing, B.M. and D.K.; visualization, D.K.; supervision, B.M. and D.K. All authors have read and agreed to the published version of the manuscript.

Funding: This research was supported by the Silesian University of Technology statutory financial support No. BK: 07/010/BK_24/1034 (BK-289/RIB1/2024).

Institutional Review Board Statement: Not applicable.

Informed Consent Statement: Not applicable.

Data Availability Statement: To evaluate the performance of the proposed method, the MIT-BIH Atrial Fibrillation Database was used [42] <https://physionet.org/content/afdb/1.0.0/> (accessed on 24 June 2024).

Conflicts of Interest: The authors declare that they have no competing interests.

Abbreviations

The following abbreviations are used in this manuscript:

AFIB	Atrial Fibrillation
ECG	Electrocardiography/Electrocardiogram
CNN	Convolution Neural Network
AFIB-NET	CNN for AFIB Detection
AFDB	MIT-BIH Atrial Fibrillation Database
ROC	Receiver Operating Characteristic
AI	Artificial Intelligence
HOSA	Higher-Order Statistics Analysis
DL	Deep Learning
DNN	Deep Neural Network
RNN	Recurrent Neural Network
LSTM	Long Short-Term Memory Network
CNN + LSTM	Hybrid (CNN+LSTM) Network
HOS	Higher-Order Statistics
SRN	Signal-To-Noise Ratio
EEG	Electroencephalogram
EMG	Electromyogram
GNN	GoogLeNet Network
AFL	Atrial Flutter
J	Nodal (Junctional) Rhythm
FFT	Fast Fourier Transform
MBS	MiniBatch Size
ILR	Initial Learning Rate
TPR	True Positive Rate (Sensitivity, Recall)
TNR	True Negative Rate (Specificity)
PPV	Precision of Positive Predictive Value
NPV	Precision of Negative Predictive Value
PV	Prevalence

ACC	Accuracy
LR+	Likelihood Ratio of Positive Value
LR-	Likelihood Ratio of Negative Value
AUC	Area Under Receiver Operating Characteristic (ROC)
TP	True Positive
FN	False Negative
FP	False Positive
TN	True Negative

References

- Kornej, J.; Börschel, C.S.; Benjamin, E.J.; Schnabel, R.B. Epidemiology of Atrial Fibrillation in the 21st Century. *Circ. Res.* **2020**, *127*, 4–20. [[CrossRef](#)]
- Hindricks, G.; Potpara, T.; Dagres, N.; Arbelo, E.; Bax, J.J.; Blomström-Lundqvist, C.; Boriani, G.; Castella, M.; Dan, G.A.; Dilaveris, P.E.; et al. 2020 ESC Guidelines for the diagnosis and management of atrial fibrillation developed in collaboration with the European Association for Cardio-Thoracic Surgery (EACTS): The Task Force for the diagnosis and management of atrial fibrillation of the European Society of Cardiology (ESC) Developed with the special contribution of the European Heart Rhythm Association (EHRA) of the ESC. *Eur. Heart J.* **2020**, *42*, 373–498. [[CrossRef](#)]
- Miyasaka, Y.; Barnes, M.E.; Gersh, B.J.; Cha, S.S.; Bailey, K.R.; Abhayaratna, W.P.; Seward, J.B.; Tsang, T.S. Secular Trends in Incidence of Atrial Fibrillation in Olmsted County, Minnesota, 1980 to 2000, and Implications on the Projections for Future Prevalence. *Circulation* **2006**, *114*, 119–125. [[CrossRef](#)]
- Krijthe, B.P.; Kunst, A.; Benjamin, E.J.; Lip, G.Y.H.; Franco, O.H.; Hofman, A.; Wittteman, J.C.M.; Stricker, B.H.; Heeringa, J. Projections on the number of individuals with atrial fibrillation in the European Union, from 2000 to 2060. *Eur. Heart J.* **2013**, *34*, 2746–2751. [[CrossRef](#)]
- Cheniti, G.; Vlachos, K.; Pambrun, T.; Hooks, D.; Frontera, A.; Takigawa, M.; Bourier, F.; Kitamura, T.; Lam, A.; Martin, C.; et al. Atrial Fibrillation Mechanisms and Implications for Catheter Ablation. *Front. Physiol.* **2018**, *9*, 1458. [[CrossRef](#)]
- Veenhuyzen, G.D. Atrial fibrillation. *Can. Med. Assoc. J.* **2004**, *171*, 755–760. [[CrossRef](#)]
- Iwasaki, Y.K.; Nishida, K.; Kato, T.; Nattel, S. Atrial Fibrillation Pathophysiology. *Circulation* **2011**, *124*, 2264–2274. [[CrossRef](#)]
- Jekova, I.; Christov, I.; Krasteva, V. Atrioventricular Synchronization for Detection of Atrial Fibrillation and Flutter in One to Twelve ECG Leads Using a Dense Neural Network Classifier. *Sensors* **2022**, *22*, 6071. [[CrossRef](#)]
- Steinberg, J.S.; O’Connell, H.; Li, S.; Ziegler, P.D. Thirty-Second Gold Standard Definition of Atrial Fibrillation and Its Relationship With Subsequent Arrhythmia Patterns. *Circ. Arrhythmia Electrophysiol.* **2018**, *11*, 522. [[CrossRef](#)]
- Odutayo, A.; Wong, C.X.; Hsiao, A.J.; Hopewell, S.; Altman, D.G.; Emdin, C.A. Atrial fibrillation and risks of cardiovascular disease, renal disease, and death: Systematic review and meta-analysis. *BMJ* **2016**, *354*, i4482. [[CrossRef](#)]
- Wathen, J.E.; Rewers, A.B.; Yetman, A.T.; Schaffer, M.S. Accuracy of ECG interpretation in the pediatric emergency department. *Ann. Emerg. Med.* **2005**, *46*, 507–511. [[CrossRef](#)] [[PubMed](#)]
- Raghunath, S.; Pfeifer, J.M.; Ulloa-Cerna, A.E.; Nemani, A.; Carbonati, T.; Jing, L.; vanMaanen, D.P.; Hartzel, D.N.; Ruhl, J.A.; Lagerman, B.F.; et al. Deep Neural Networks Can Predict New-Onset Atrial Fibrillation From the 12-Lead ECG and Help Identify Those at Risk of Atrial Fibrillation-Related Stroke. *Circulation* **2021**, *143*, 1287–1298. [[CrossRef](#)] [[PubMed](#)]
- Ghosh, S.K.; Tripathy, R.K.; Paternina, M.R.A.; Arrieta, J.J.; Zamora-Mendez, A.; Naik, G.R. Detection of Atrial Fibrillation from Single Lead ECG Signal Using Multirate Cosine Filter Bank and Deep Neural Network. *J. Med. Syst.* **2020**, *44*, 2370. [[CrossRef](#)] [[PubMed](#)]
- Xia, Y.; Wulan, N.; Wang, K.; Zhang, H. Detecting atrial fibrillation by deep convolutional neural networks. *Comput. Biol. Med.* **2018**, *93*, 84–92. [[CrossRef](#)] [[PubMed](#)]
- Nurmaini, S.; Tondas, A.E.; Darmawahyuni, A.; Rachmatullah, M.N.; Partan, R.U.; Firdaus, F.; Tutuko, B.; Pratiwi, F.; Juliano, A.H.; Khoirani, R. Robust detection of atrial fibrillation from short-term electrocardiogram using convolutional neural networks. *Future Gener. Comput. Syst.* **2020**, *113*, 304–317. [[CrossRef](#)]
- Sun, Y.; Shen, J.; Jiang, Y.; Huang, Z.; Hao, M.; Zhang, X. MMA-RNN: A multi-level multi-task attention-based recurrent neural network for discrimination and localization of atrial fibrillation. *Biomed. Signal Process. Control* **2024**, *89*, 105747. [[CrossRef](#)]
- Sujadevi, V.G.; Soman, K.P.; Vinayakumar, R. Real-Time Detection of Atrial Fibrillation from Short Time Single Lead ECG Traces Using Recurrent Neural Networks. In *Intelligent Systems Technologies and Applications, Proceedings of the Third International Symposium on Intelligent Systems Technologies and Applications (ISTA’17), Manipal, India, 13–16 September 2017*; Thampi, S.M., Mitra, S., Mukhopadhyay, J., Li, K.C., James, A.P., Berretti, S., Eds.; Springer: Cham, Switzerland, 2018; pp. 212–221.
- Gündüz, A.F.; Talu, M.F. Atrial fibrillation classification and detection from ECG recordings. *Biomed. Signal Process. Control* **2023**, *82*, 104531. [[CrossRef](#)]
- Faust, O.; Shenfield, A.; Kareem, M.; San, T.R.; Fujita, H.; Acharya, U.R. Automated detection of atrial fibrillation using long short-term memory network with RR interval signals. *Comput. Biol. Med.* **2018**, *102*, 327–335. [[CrossRef](#)] [[PubMed](#)]
- Murat, F.; Sadak, F.; Yildirim, O.; Talo, M.; Murat, E.; Karabatak, M.; Demir, Y.; Tan, R.S.; Acharya, U.R. Review of Deep Learning-Based Atrial Fibrillation Detection Studies. *Int. J. Environ. Res. Public Health* **2021**, *18*, 11302. [[CrossRef](#)]

21. Iftene, A.; Burlacu, A.; Gifu, D. Atrial Fibrillation Detection Based on Deep Learning Models. *Procedia Comput. Sci.* **2022**, *207*, 3752–3760. [CrossRef]
22. Subramanyan, L.; Ganesan, U. A novel deep neural network for detection of Atrial Fibrillation using ECG signals. *Knowl.-Based Syst.* **2022**, *258*, 109926. [CrossRef]
23. Petmezas, G.; Haris, K.; Stefanopoulos, L.; Kilintzis, V.; Tzavelis, A.; Rogers, J.A.; Katsaggelos, A.K.; Maglaveras, N. Automated Atrial Fibrillation Detection using a Hybrid CNN-LSTM Network on Imbalanced ECG Datasets. *Biomed. Signal Process. Control* **2021**, *63*, 102194. [CrossRef]
24. Ebrahimi, Z.; Loni, M.; Daneshlab, M.; Gharehbaghi, A. A review on deep learning methods for ECG arrhythmia classification. *Expert Syst. Appl.* **2020**, *7*, 100033. [CrossRef]
25. Ansari, Y.; Mourad, O.; Qaraqe, K.; Serpedin, E. Deep learning for ECG Arrhythmia detection and classification: An overview of progress for period 2017–2023. *Front. Physiol.* **2023**, *14*, 1246746. [CrossRef]
26. Chua, K.C.; Chandran, V.; Acharya, U.R.; Lim, C.M. Application of higher order statistics/spectra in biomedical signals—A review. *Med. Eng. Phys.* **2010**, *32*, 679–689. [CrossRef]
27. Nikias, C.; Mendel, J. Signal processing with higher-order spectra. *IEEE Signal Process. Mag.* **1993**, *10*, 10–37. [CrossRef]
28. Mendel, J. Tutorial on higher-order statistics (spectra) in signal processing and system theory: Theoretical results and some applications. *Proc. IEEE* **1991**, *79*, 278–305. [CrossRef]
29. Sigl, J.C.; Chamoun, N.G. An introduction to bispectral analysis for the electroencephalogram. *J. Clin. Monit.* **1994**, *10*, 392–404. [CrossRef]
30. Khoshnevis, S.A.; Sankar, R. Applications of Higher Order Statistics in Electroencephalography Signal Processing: A Comprehensive Survey. *IEEE Rev. Biomed. Eng.* **2020**, *13*, 169–183. [CrossRef]
31. Mahmoodian, N.; Haddadnia, J.; Illanes, A.; Boese, A.; Friebe, M. Seizure prediction with cross-higher-order spectral analysis of EEG signals. *Signal Image Video Process.* **2020**, *14*, 821–828. [CrossRef]
32. Sezgin, N. Analysis of EMG Signals in Aggressive and Normal Activities by Using Higher-Order Spectra. *Sci. World J.* **2012**, *2012*, 478952. [CrossRef]
33. Kotriwar, Y.; Kachhara, S.; Harikrishnan, K.P.; Ambika, G. Higher order spectral analysis of ECG signals. *arXiv* **2018**, arXiv:1809.08451.
34. Martis, R.J.; Acharya, U.R.; Prasad, H.; Chua, C.K.; Lim, C.M.; Suri, J.S. Application of higher order statistics for atrial arrhythmia classification. *Biomed. Signal Process. Control* **2013**, *8*, 888–900. [CrossRef]
35. Liu, S.; Shao, J.; Kong, T.; Malekian, R. ECG Arrhythmia Classification using High Order Spectrum and 2D Graph Fourier Transform. *Appl. Sci.* **2020**, *10*, 4741. [CrossRef]
36. Deka, B.; Deka, D. Nonlinear analysis of heart rate variability signals in meditative state: A review and perspective. *Biomed. Eng. Online* **2023**, *22*, 35. [CrossRef]
37. Xu, J.; Ye, P.; Li, Q.; Du, H.; Liu, Y.; Doermann, D. Blind Image Quality Assessment Based on High Order Statistics Aggregation. *IEEE Trans. Image Process.* **2016**, *25*, 4444–4457. [CrossRef]
38. Sanaullah, M. A Review of Higher Order Statistics and Spectra in Communication Systems. *Glob. J. Sci. Front. Res.* **2013**, 31–50. [CrossRef]
39. Ould-Baba, H.; Robin, V.; Antoni, J. Concise formulae for the cumulant matrices of a random vector. *Linear Algebra Its Appl.* **2015**, *485*, 392–416. [CrossRef]
40. La Rosa, J.J.G.d.; Agüera-Pérez, A.; Palomares-Salas, J.C.; Moreno-Muñoz, A. Higher-order statistics: Discussion and interpretation. *Measurement* **2013**, *46*, 2816–2827. [CrossRef]
41. Szegedy, C.; Liu, W.; Jia, Y.; Sermanet, P.; Reed, S.; Anguelov, D.; Erhan, D.; Vanhoucke, V.; Rabinovich, A. Going Deeper with Convolutions. *arXiv* **2014**, arXiv:1409.4842. <https://doi.org/10.48550/arXiv.1409.4842>
42. Goldberger, A.L.; Amaral, L.A.N.; Glass, L.; Hausdorff, J.M.; Ivanov, P.C.; Mark, R.G.; Mietus, J.E.; Moody, G.B.; Peng, C.K.; Stanley, H.E. PhysioBank, PhysioToolkit, and PhysioNet: Components of a New Research Resource for Complex Physiologic Signals. *Circulation* **2000**, *101*, e215–e220. [CrossRef] [PubMed]
43. Swami, A. HOSA—Higher Order Spectral Analysis Toolbox. MATLAB Central File Exchange. 2023. Available online: <https://www.mathworks.com/matlabcentral/fileexchange/3013-hosa-higher-order-spectral-analysis-toolbox> (accessed on 19 December 2023).
44. Alcaraz, R.; Rieta, J.J. Surface ECG organization analysis to predict paroxysmal atrial fibrillation termination. *Comput. Biol. Med.* **2009**, *39*, 697–706. [CrossRef]
45. Castells, F.; Rieta, J.J.; Millet, J.; Zarzoso, V. Spatiotemporal Blind Source Separation Approach to Atrial Activity Estimation in Atrial Tachyarrhythmias. *IEEE Trans. Biomed. Eng.* **2005**, *52*, 258–267. [CrossRef]
46. Diaz, J.; Escalona, O.; Castro, N.; Anderson, J.; Glover, B.; Manoharan, G. Predicting transthoracic defibrillation shocks outcome in the cardioversion of atrial fibrillation employing support vector machines. In Proceedings of the 2010 Computing in Cardiology, Belfast, UK, 26–29 September 2010; pp. 741–744.
47. Llinares, R.; Igual, J. Exploiting periodicity to extract the atrial activity in atrial arrhythmias. *EURASIP J. Adv. Signal Process.* **2011**, *2011*, 1176. [CrossRef]
48. Petrutiu, S.; Ng, J.; Nijm, G.M.; Al-Angari, H.; Swiryn, S.; Sahakian, A.V. Atrial fibrillation and waveform characterization. *IEEE Eng. Med. Biol. Mag.* **2006**, *25*, 24–30. [CrossRef]

49. Stridh, M.; Sornmo, L.; Meurling, C.J.; Olsson, S.B. Sequential Characterization of Atrial Tachyarrhythmias Based on ECG Time-Frequency Analysis. *IEEE Trans. Biomed. Eng.* **2004**, *51*, 100–114. [[CrossRef](#)]
50. Stridh, M.; Bollmann, A.; Olsson, S.B.; Sornmo, L. Detection and feature extraction of atrial tachyarrhythmias. *IEEE Eng. Med. Biol. Mag.* **2006**, *25*, 31–39. [[CrossRef](#)]
51. Hayes, M.H. *Statistical Digital Signal Processing and Modeling*, 1st ed.; John Wiley & Sons, Inc.: Hoboken, NJ, USA, 1996.
52. Stoica, P.; Moses, R.L. *Spectral Analysis of Signals/Petre Stoica and Randolph Moses*; Pearson/Prentice Hall: Upper Saddle River, NJ, USA, 2005.
53. Grimes, D.A.; Schulz, K.F. Refining clinical diagnosis with likelihood ratios. *Lancet* **2005**, *365*, 1500–1505. [[CrossRef](#)]
54. Peng, P.; Coyle, A.; Newgard, C.D. Likelihood Ratios for the Emergency Physician. *Acad. Emerg. Med.* **2018**, *25*, 958–965. [[CrossRef](#)]
55. Junge, M.R.J.; Dettori, J.R. ROC Solid: Receiver Operator Characteristic (ROC) Curves as a Foundation for Better Diagnostic Tests. *Glob. Spine J.* **2017**, *8*, 424–429. [[CrossRef](#)]
56. Osowski, S.; Hoai, L.T.; Markiewicz, T. Support Vector Machine-Based Expert System for Reliable Heartbeat Recognition. *IEEE Trans. Biomed. Eng.* **2004**, *51*, 582–589. [[CrossRef](#)]
57. Mousavi, S.; Afghah, F.; Razi, A.; Acharya, U.R. ECGNET: Learning Where to Attend for Detection of Atrial Fibrillation with Deep Visual Attention. In Proceedings of the 2019 IEEE EMBS International Conference on Biomedical & Health Informatics (BHI), Chicago, IL, USA, 19–22 May 2019; pp. 1–4. [[CrossRef](#)]
58. Radhakrishnan, T.; Karhade, J.; Ghosh, S.; Muduli, P.; Tripathy, R.; Acharya, U.R. AFCNNet: Automated detection of AF using chirplet transform and deep convolutional bidirectional long short term memory network with ECG signals. *Comput. Biol. Med.* **2021**, *137*, 104783. [[CrossRef](#)]
59. Yang, W.; Wang, D.; Fan, W.; Zhang, G.; Li, C.; Liu, T. Automated atrial fibrillation and ventricular fibrillation recognition using a multi-angle dual-channel fusion network. *Artif. Intell. Med.* **2023**, *145*, 102680. [[CrossRef](#)]
60. Marsanova, L.; Nemcova, A.; Smisek, R.; Vitek, M.; Smital, L. Single-Feature Method for Fast Atrial Fibrillation Detection in ECG Signals. In Proceedings of the 2020 Computing in Cardiology, Rimini, Italy, 13–16 September 2020; pp. 1–4. [[CrossRef](#)]
61. Wang, J.; Wang, P.; Wang, S. Automated detection of atrial fibrillation in ECG signals based on wavelet packet transform and correlation function of random process. *Biomed. Signal Process. Control* **2020**, *55*, 101662. [[CrossRef](#)]
62. Kumar, M.; Pachori, R.B.; Rajendra Acharya, U. Automated diagnosis of atrial fibrillation ECG signals using entropy features extracted from flexible analytic wavelet transform. *Biocybern. Biomed. Eng.* **2018**, *38*, 564–573. [[CrossRef](#)]
63. Tripathy, R.K.; Paternina, M.R.A.; Arrieta, J.G.; Pattanaik, P. Automated Detection Of Atrial Fibrillation Ecg Signals Using Two Stage Vmd And Atrial Fibrillation Diagnosis Index. *J. Mech. Med. Biol.* **2017**, *17*, 1740044. [[CrossRef](#)]
64. Asgari, S.; Mehrnia, A.; Moussavi, M. Automatic detection of atrial fibrillation using stationary wavelet transform and support vector machine. *Comput. Biol. Med.* **2015**, *60*, 132–142. [[CrossRef](#)]
65. Lee, J.; Reyes, B.A.; McManus, D.D.; Maitas, O.; Chon, K.H. Atrial Fibrillation Detection Using an iPhone 4S. *IEEE Trans. Biomed. Eng.* **2013**, *60*, 203–206. [[CrossRef](#)]
66. Huang, C.; Ye, S.; Chen, H.; Li, D.; He, F.; Tu, Y. A Novel Method for Detection of the Transition Between Atrial Fibrillation and Sinus Rhythm. *IEEE Trans. Biomed. Eng.* **2011**, *58*, 1113–1119. [[CrossRef](#)]
67. Tateno, K.; Glass, L. Automatic detection of atrial fibrillation using the coefficient of variation and density histograms of RR and dRR intervals. *Med. Biol. Eng. Comput.* **2001**, *39*, 664–671. [[CrossRef](#)]

Disclaimer/Publisher’s Note: The statements, opinions and data contained in all publications are solely those of the individual author(s) and contributor(s) and not of MDPI and/or the editor(s). MDPI and/or the editor(s) disclaim responsibility for any injury to people or property resulting from any ideas, methods, instructions or products referred to in the content.